Synthesis and characterization of LiFePO$_4$–carbon nanofiber–carbon nanotube composites prepared by electrospinning and thermal treatment as a cathode material for lithium-ion batteries

Changhuan Zhang, Lan Yao, Yiping Qiu
Shanghai Key Laboratory of Advanced Micro and Nano Textile Materials, College of Textiles, Donghua University, Shanghai 201620, China
Correspondence to: Y. Qiu (E-mail: ypqiu@dhu.edu.cn)

ABSTRACT: Binder-free LiFePO$_4$–carbon nanofiber (CNF)–multiwalled carbon nanotube (MWCNT) composites were prepared by electrospinning and thermal treatment to form a freestanding conductive web that could be used directly as a battery cathode without addition of a conductive material and polymer binder. The thermal decomposition behavior of the electrospun LiFePO$_4$ precursor–polyacrylonitrile (PAN) and LiFePO$_4$ precursor–PAN–MWCNT composites before and after stabilization were studied with thermogravimetric analysis (TGA)/differential scanning calorimetry and TGA/differential thermal analysis, respectively. The structure, morphology, and carbon content of the LiFePO$_4$–CNF and LiFePO$_4$–CNF–MWCNT composites were determined by X-ray diffraction, high-resolution transmission electron microscopy, Raman spectroscopy, scanning electron microscopy, and elemental analysis. The electrochemical properties of the LiFePO$_4$–CNF and LiFePO$_4$–CNF–MWCNT composite cathodes were measured by charge–discharge tests and electrochemical impedance spectroscopy. The synthesized composites with MWCNTs exhibited better rate performances and more stable cycle performances than the LiFePO$_4$–CNF composites; this was due to the increase in electron transfer and lithium-ion diffusion within the composites loaded with MWCNTs. The composites containing 0.15 wt % MWCNTs delivered a proper initial discharge capacity of 156.7 mA h g^{-1} at 0.5 C rate and a stable cycle ability on the basis of the weight of the active material, LiFePO$_4$. © 2015 Wiley Periodicals, Inc. J. Appl. Polym. Sci. **2016**, *133*, 43001.

INTRODUCTION

Lithium-ion batteries (LIBs) have been applied in home electronics and large-scale energy storage devices.[1,2] Thus, cathode materials for LIBs with a high specific capacity and high rate capability are in demand.[3–6] The ordered olivine-type structure LiFePO$_4$ has attracted much attention as a storage cathode material for LIBs because of its relatively high theoretical specific capacity, an appropriate charge–discharge flat plateau, excellent structural stability, high thermal stability, and its environmental compatibility and low cost.[7–10] However, olivine LiFePO$_4$ has two intrinsic disadvantages, namely a poor electronic conductivity ($\sim 10^{-9}$ to 10^{-10} s/cm) and slow lithium-ion diffusion rate ($\sim 10^{-14}$ cm^2/s) at room temperature[11,12]; this restricts its performance and sets an obstacle for its wider application. Therefore, much attention has been paid to improve LiFePO$_4$-based materials to overcome these shortcomings. The performance of the LiFePO$_4$-based material has been improved by the reduction and homogenization of the material size,[13–16]

customization of the material morphology,[17–19] doping with foreign cations,[20–24] and modification with conductive materials (carbon, conducting polymer, Ag, etc.).[25–32] In particular, modification with carbon materials has attracted much interest because of the abundance of carbon sources, such as carbon nanotubes (CNTs).

CNTs, as a very promising conductive additive, can either provide more routes or accelerate the speed for the transportation of electrons and lithium ions in cathodes through the production of a highly conductive network in the cathodes because of its fibrous morphology, high contact efficiency, excellent electrical conductivity, and high surface area.[33,34] Until now, many synthesis strategies have been attempted to prepare LiFePO$_4$–CNT composites; these include a solid-state reaction, hydrothermal reaction, liquid mixing, ball milling, and sol–gel method.[35–39] However, most previous studies have used powder materials for which polymer binders are necessary to hold active material on the substrate; this leads to a limited improvement

Table I. Weight Ratios of the MWCNTs, PAN, LiFePO$_4$ Precursor, and DMF in the Electrospinning Solution

Sample	MWCNTs (wt %)	PAN (wt %)	LiFePO$_4$ precursor (wt %)	DMF (wt %)
LiFePO$_4$ precursor–PAN	0	8	8	84.00
LiFePO$_4$ precursor–PAN–MWCNT1	0.05	8	8	83.95
LiFePO$_4$ precursor–PAN–MWCNT2	0.10	8	8	83.90
LiFePO$_4$ precursor–PAN–MWCNT3	0.15	8	8	83.85
LiFePO$_4$ precursor–PAN–MWCNT4	0.20	8	8	83.80
LiFePO$_4$ precursor–PAN–MWCNT5	0.25	8	8	83.75
LiFePO$_4$ precursor–PAN–MWCNT6	0.30	8	8	83.70

in the performance. This can be solved by the adoption of the electrospinning of precursor materials containing uniformly dispersed CNTs into nanofiber webs followed by thermal treatments to form binder-free composites. Toprakci et al.[40] reported functionalized CNT-loaded electrospun LiFePO$_4$/carbon composite nanofibers. However, in their study, the relationship between the properties and amount of multiwalled carbon nanotubes (MWCNTs) was not systematically studied.

In this study, we describe a facile route for fabricating binder-free LiFePO$_4$–carbon nanofiber (CNF)–MWCNT composites. The syntheses process involved electrospinning LiFePO$_4$ precursor–polyacrylonitrile (PAN)–MWCNT nanofiber webs followed by thermal treatment. Nanosized LiFePO$_4$ materials were synthesized in situ with the encapsulation of the CNF matrix; simultaneously, the MWCNTs were embedded in the LiFePO$_4$–CNF matrix. The CNF structure generated by electrospinning and thermal treatment could also promote fast electron transfer along the fiber axial direction; this prevented the active material from aggregating and overcrystallizing, and the MWCNTs were chosen as a conductive additive to form a well-connected conductive network and provide a conduction path.

EXPERIMENTAL

Preparation of the Composites

The LiFePO$_4$–CNF–MWCNT composites were synthesized through electrospinning and subsequent thermal treatments. All of the chemicals used in this study were analytical grade. First, the MWCNTs (length = 1–2 μm, main range of diameter = 10–20 nm, Shenzhen Nanotech Port Co., Ltd.) were dispersed in N,N-dimethylformamide [DMF; analytical reagent (AR), Shanghai Runjie Chemical Reagent Co., Ltd.] with sufficient ultrasonication for at least 6 h and then vigorous stirring to form a homogeneous solution. Second, PAN (typical weight-average molecular weight = 150,000; Sigma-Aldrich) with a ratio of 8 wt % of the solution, was added and stirred magnetically for 24 h at 60°C to obtain a uniform mixture solution. Finally, lithium acetate (LiCOOCH$_3$; 99.95% trace metal basis, Sigma-Aldrich), iron(II) acetate [Fe(COOCH$_3$)$_2$; 95% trace metals basis, Sigma-Aldrich], and phosphoric acid (H$_3$PO$_4$; 99.999% trace metal basis, Sigma-Aldrich) in a stoichiometric molar ratio of 1:1:1 with a concentration of 8 wt % were successively dissolved in a mixture solution under magnetic stirring. The previ-

ous solution was stirred for 24 h to obtain an electrospinning solution. In this study, samples with MWCNT concentrations of 0.05, 0.10, 0.15, 0.20, 0.25, and 0.30 wt % were prepared. Table I shows the weight ratios of the MWCNTs, PAN, LiFePO$_4$ precursors, and DMF in the electrospinning solutions.

Electrospinning solutions were placed in a 10-mL syringe with 0.51-mm metal needles. A variable high-voltage power supply (EST804A, Tianjin Dongwen, China) was used to provide an electrical potential of around 23 kV for electrospinning with a 1 mL/h feeding rate and a 15-cm tip-to-collector distance. The fibers were collected on a flat and nonstick aluminum foil sheet.

The peeled electrospun LiFePO$_4$ precursor–PAN–MWCNT composites was placed in a furnace for a thermal treatment of stabilization at 280°C for 4 h in air at a heating rate of 2°C/min followed by carbonization at 800°C for 14 h in argon (Ar) at a heating rate of 2°C/min. After natural cooling to room temperature, LiFePO$_4$–CNF–MWCNT composites were obtained for later use. This process is illustrated in Figure 1. For comparison, LiFePO$_4$–CNF composites were prepared without the addition of MWCNTs with the same procedure.

Characterization of the Samples

The thermal decomposition behavior of the electrospun LiFePO$_4$ precursor–PAN and LiFePO$_4$ precursor–PAN–MWCNT composites were investigated by thermogravimetric analysis (TGA)/differential scanning calorimetry (DSC; SDT-Q600, TA Instruments); this was performed at a heating rate of 10°C/min from room temperature to 600°C in flowing air and nitrogen (N$_2$). The thermal decomposition behavior of these composites stabilized at 280°C for 4 h at a heating rate of 2°C/min were studied with TGA/differential thermal analysis (DTA; SDT-Q600, TA Instruments), which was performed at a heating rate of 10°C/min from room temperature to 900°C in flowing N$_2$. The morphologies of the electrospun webs before and after thermal treatment were evaluated by scanning electron microscopy (Quanta 250, FEI) at 10 kV. The carbon contents of the LiFePO$_4$–CNF and LiFePO$_4$–CNF–MWCNT composites were determined by elemental analysis (Elmentar, Vario EL III, Germany). The crystal structures of the electrospun webs after the thermal treatment were carried out by X-ray diffraction (XRD; λ = 1.54056 Å; D/max-2500PC XRD system, Cu Kα, Rigaku, Japan) in the 2θ range 10–60° with 2θ step scan intervals of
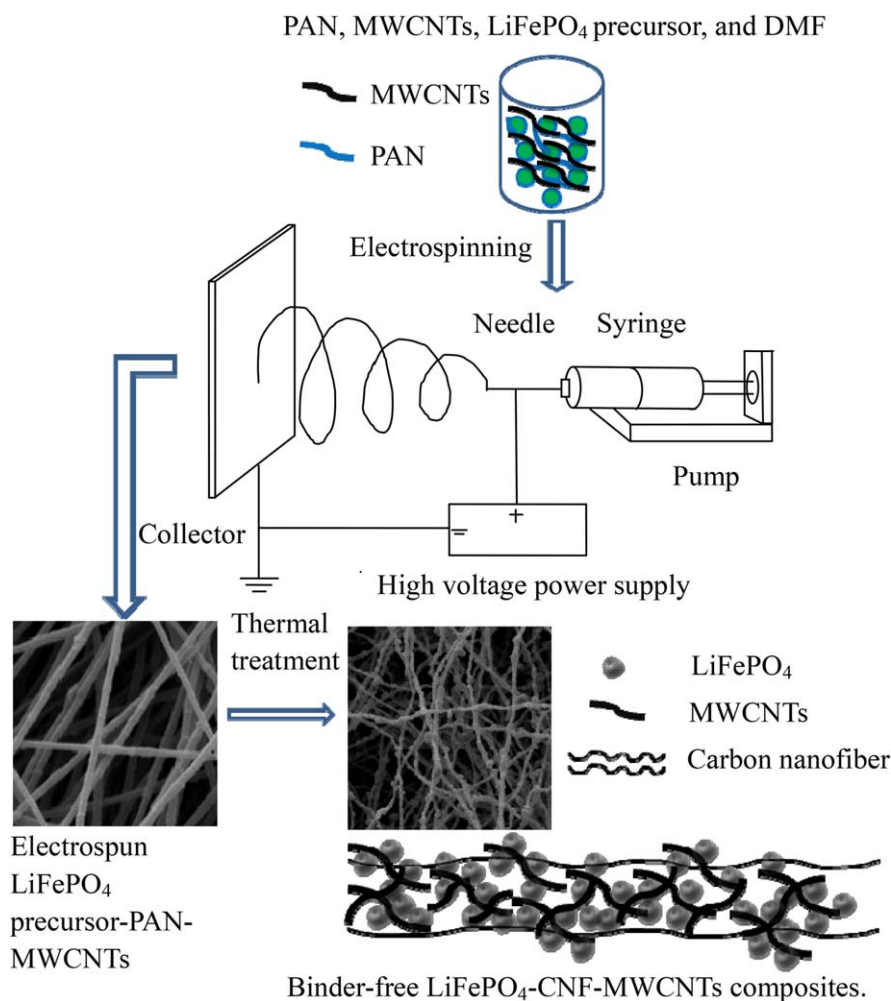
Figure 1. Schematic illustration of the preparation of the $LiFePO_4$–CNF–MWCNT composites. [Color figure can be viewed in the online issue, which is available at wileyonlinelibrary.com.]

$0.02°$ and a count time of 0.06 s per step. The fine structures of the $LiFePO_4$–CNF and $LiFePO_4$–CNF–MWCNT3 composites were observed with high-resolution transmission electron microscopy (HRTEM; 2100F, Hitachi, Japan). The structural variations of the carbonaceous material in the electrospun webs, CNFs, MWCNTs, and $LiFePO_4$–CNF and $LiFePO_4$–CNF–MWCNT composites were identified by Raman spectroscopy (Raman, Invia-Reflex, Renishaw Raman Microscopy, Britain).

Electrochemical Characterization

The $LiFePO_4$–CNF and $LiFePO_4$–CNF–MWCNT composites formed freestanding porous paper, and they were directly used as cathodes without the addition of any polymer binder and conductive material. The current collector used aluminum foil. CR2032-type coin cells were fabricated with lithium metal as the counter electrode in an Ar-filled glovebox with contents of H_2O and O_2 of less than 0.1 ppm. The electrolyte used consisted of a 1 mol/L solution of lithium hexafluorophosphate ($LiPF_6$) in a mixture (1:1 w/w) of ethylene carbonate and dimethyl carbonate. A microporous polypropylene film (Celgard 2400) was used as the separator. The galvanostatic charge–discharge characteristics of the cathode were performed in the potential range 2.5–4.2 V versus Li/Li^+ with a battery testing system (CT2001A, LAND, China). The cycle performance was evaluated at a constant current of 85 mA/g (0.5 C, where 1 C = 170 mA/g), and the C-rate performance was evaluated at various current rates (0.05–2 C) through cycling for five times at each rate. The electrochemical impedance spectroscopy (EIS) measurements were performed on an electrochemical working station (CHI650C, China). The EIS spectra were obtained in the frequency range 10^5 to 10^{-2} Hz with an amplitude potential of 5 mV. All of the electrochemical experiments were conducted at room temperature, and all capacity values were calculated on the basis of the weight of the active material $LiFePO_4$.

RESULTS AND DISCUSSION

Thermal Decomposition

Figure 2(a,b) shows the TGA/DSC curves of the electrospun $LiFePO_4$ precursor–PAN and $LiFePO_4$ precursor–PAN–MWCNT3 composites in air. Figure 2(c,d) shows the TGA/DSC curves of these composites in N_2. Figure 3(a,b) shows the TGA/DTA curves of these composites stabilized at 280°C for 4 h at a heating rate of 2°C/min in N_2. Several endothermic and exothermic peaks are shown in the DSC and DTA curves, and
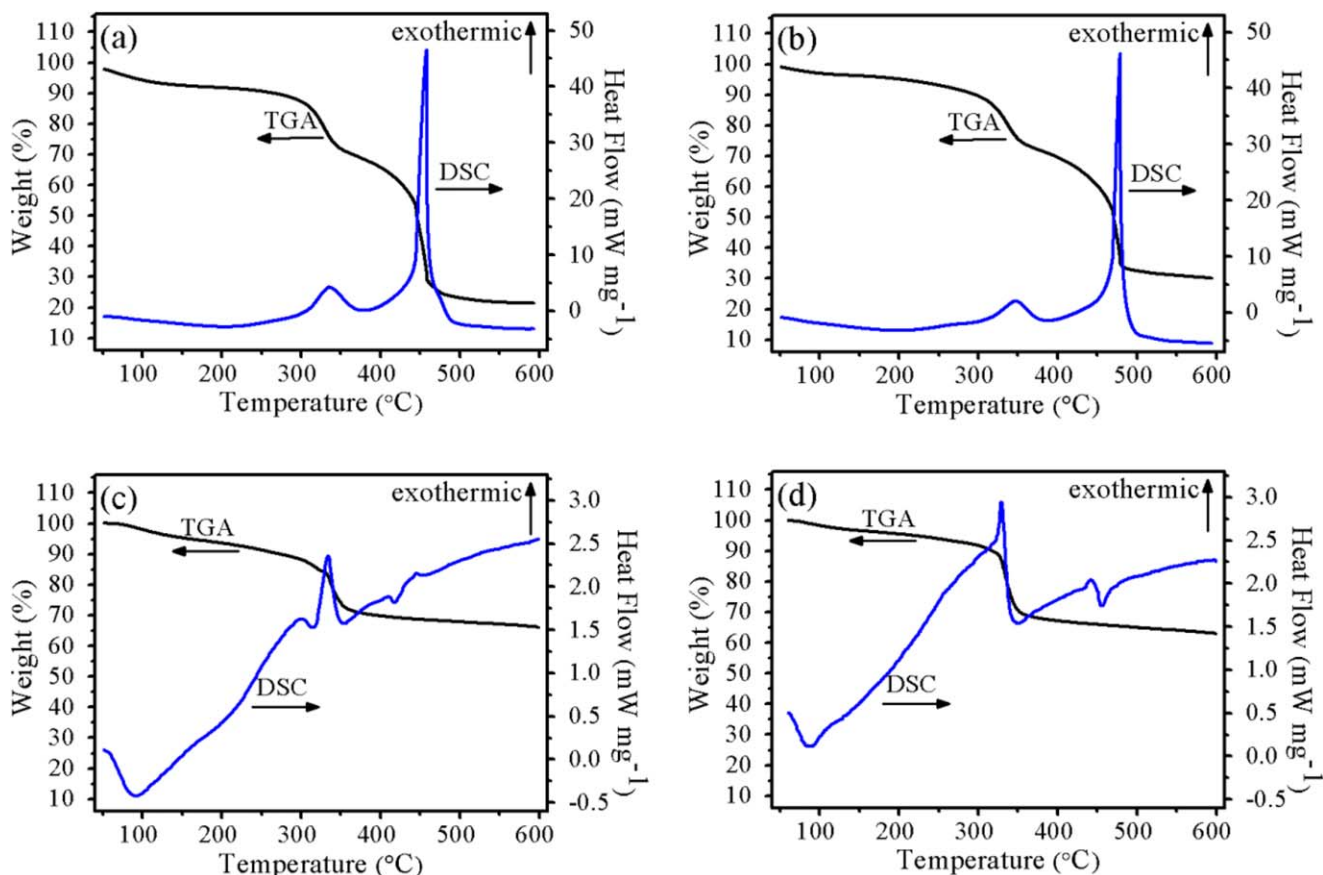
Figure 2. TGA/DSC curves of the (a) electrospun LiFePO$_4$ precursor–PAN and (b) electrospun LiFePO$_4$ precursor–PAN–MWCNT3 composites in air and (c) electrospun LiFePO$_4$ precursor–PAN and (d) electrospun LiFePO$_4$ precursor–PAN–MWCNT3 composites in N$_2$ between the ambient temperature and 600°C. [Color figure can be viewed in the online issue, which is available at wileyonlinelibrary.com.]

several stages of weight loss were observed in the TGA curves. The main thermal decomposition temperatures are listed in Tables II and III.

As shown in Figure 2(a,b), TGA curves in air for the electrospun LiFePO$_4$ precursor–PAN [Figure 2(a)] and LiFePO$_4$ precursor–PAN–MWCNT3 [Figure 2(b)] were similar to the

two steps of sharp weight loss. The major weight loss occurred in the temperature ranges 300–350°C and 400–470°C. In the DSC curves, two exothermic peaks were observed at 335 and 458°C, respectively, for the electrospun LiFePO$_4$ precursor–PAN [Figure 2(a)]. This may be have been due to the oxidation reaction of the PAN at 335°C, and the formation of LiFePO$_4$
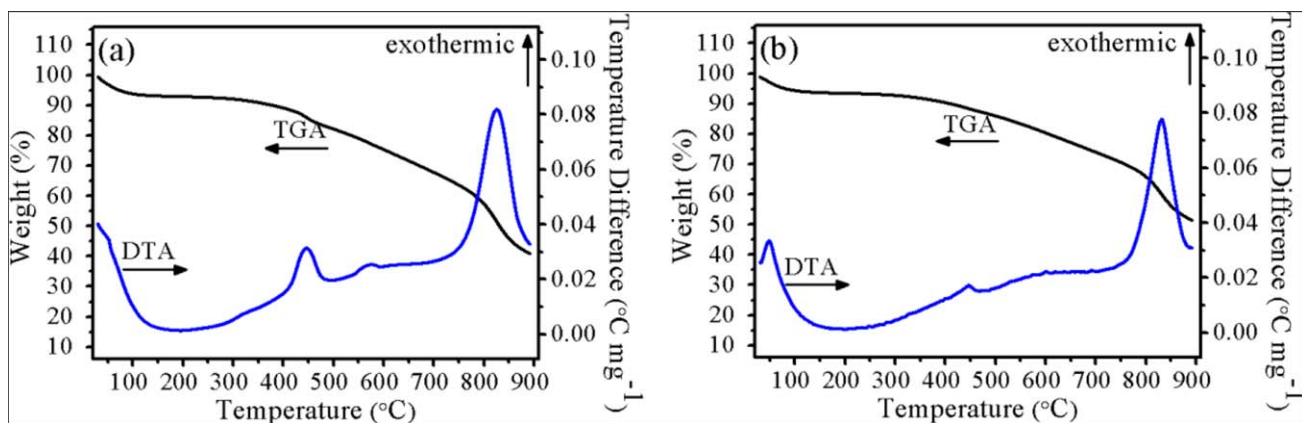

Figure 3. TGA/DTA curves of the (a) electrospun LiFePO$_4$ precursor–PAN and (b) electrospun LiFePO$_4$ precursor–PAN–MWCNT3 composites after stabilization (stabilization at 280°C for 4 h at a heating rate of 2°C/min in air) between the ambient temperature and 900°C in N$_2$. [Color figure can be viewed in the online issue, which is available at wileyonlinelibrary.com.]

Table II. Main Thermal Decomposition Temperatures in the Thermal Curves of the Electrospun LiFePO$_4$ Precursor–PAN and LiFePO$_4$ Precursor–PAN–MWCNT3 Composites in Air and in N$_2$

Sample	Air		N$_2$	
	TGA	DSC	TGA	DSC
LiFePO$_4$ precursor–PAN (°C)	300–350 and 400–470	335 and 458	300–350	300, 333, 410, and 445
LiFePO$_4$ precursor–PAN–MWCNT3 (°C)	300–350 and 400–470	345 and 478	300–350	333, 445, and 454

accompanied by the erosion of carbon at about 458°C in air. For the electrospun LiFePO$_4$ precursor–PAN–MWCNT3 [Figure 2(b)], two exothermic peaks appeared at 345 and 478°C, respectively. This indicated that the MWCNTs were only able to delay the reaction temperature of the electrospun composites.

As shown in Figure 2(c,d), in N$_2$, the two types of electrospun webs had similar TGA curves with a one-step sharp weight loss in the temperature range 300–350°C. However, their DSC curves were different from those in air with a small exothermic peak at 300°C, a strong exothermic peak at 333°C, a small endothermic peak at 410°C, and a small exothermic peak at 445°C, as shown in Figure 2(c). This was attributed to the complex reaction of the sample in N$_2$. These were mainly ascribed to the decomposition of the PAN and LiFePO$_4$ precursors and the crystallization of LiFePO$_4$.[41,42] As shown in Figure 2(d), the exothermic peak at 300°C was minimized, and the endothermic peak was shifted to 454°C in the DSC curve. This may have been due to the effect of the MWCNTs in the decomposition process. These indicated that the electrospun composites began to decompose or oxidize around 300°C and the LiFePO$_4$ crystals formed at about 445°C in N$_2$.

For the LiFePO$_4$ precursor–PAN after stabilization [Figure 3(a)] and LiFePO$_4$ precursor–PAN–MWCNTs after stabilization [Figure 3(b)], weight loss occurred in two steps, which began at about 350 and 800°C in the TGA curve. However, this gave a yield of about 45% without MWCNTs and about 52% with MWCNTs at 900°C. As shown in Figure 3(a), three exothermic peaks were observed at 446, 575, and 825°C, respectively. This may have resulted from the formation of LiFePO$_4$ crystals at 446°C, the further nucleation of LiFePO$_4$ at 575°C, and the grain growth of LiFePO$_4$ at 825°C.[41] As shown in Figure 3(b), the exothermic peak at 575°C was minimized. However, the MWCNTs served as nucleation centers and, thus, lowered the energy involved in the nucleation process, whereas the growth of the LiFePO$_4$ crystals were not influenced by the MWCNTs as the peak at 446 and 825°C were similar to those of the two composites.

Morphology Characterization

Figure 4 shows the scanning electron microscopy images of the electrospun LiFePO$_4$ precursor–PAN and electrospun LiFePO$_4$ precursor–PAN–MWCNT3 before and after thermal treatment. As shown in Figure 4, the fiber surface was smooth before thermal treatment [Figure 4(a,c)], a few various aggregate clusters were observed, and the fiber diameter and surface were nearly the same when the MWCNTs were added. This indicated that the MWCNTs did not affect the morphology of the electrospun material.

After stabilization and carbonization, all of the composites kept their networklike structures. However, the fiber diameter decreased after the thermal treatment. The fiber diameter of the electrospun composites after carbonization [Figure 4(c,f)] decreased further compared with the sample after stabilization [Figure 4(b,e)]. However, the relationship between the fiber diameter and the material performance needs to be studied further. In addition, the nanofiber morphology changed from straight to undulated after carbonization. This was attributed to the emission of a variety of gases (H$_2$O, N$_2$, CO, CO$_2$, and others) during the carbonization process in Ar; this led to a large weight loss and the formation of carbonaceous structures.[43,44] After carbonization, various aggregate clusters were observed. This was due to the conversion of the PAN matrix into CNFs after carbonization. At the same time, the LiFePO$_4$ precursors were converted to the olivine structure LiFePO$_4$, and the MWCNTs were embedded into LiFePO$_4$–CNF. The CNFs helped to limit the agglomeration of LiFePO$_4$ particles and provided a carbon coating on the surface of the LiFePO$_4$ particles. The MWCNTs also restricted the agglomeration of LiFePO$_4$ particles and provided intimate contact with the boundaries of the LiFePO$_4$ crystals.[45]

Because the precursors and MWCNTs were well dispersed in the electrospinning solution, the obtained LiFePO$_4$ particles and MWCNTs theoretically should have been uniformly embedded in the carbon fibers. As shown in Figure 4, the dispersion of the LiFePO$_4$ precursors and MWCNTs in the as-spun fibers was indeed reasonably uniform, although various aggregate clusters
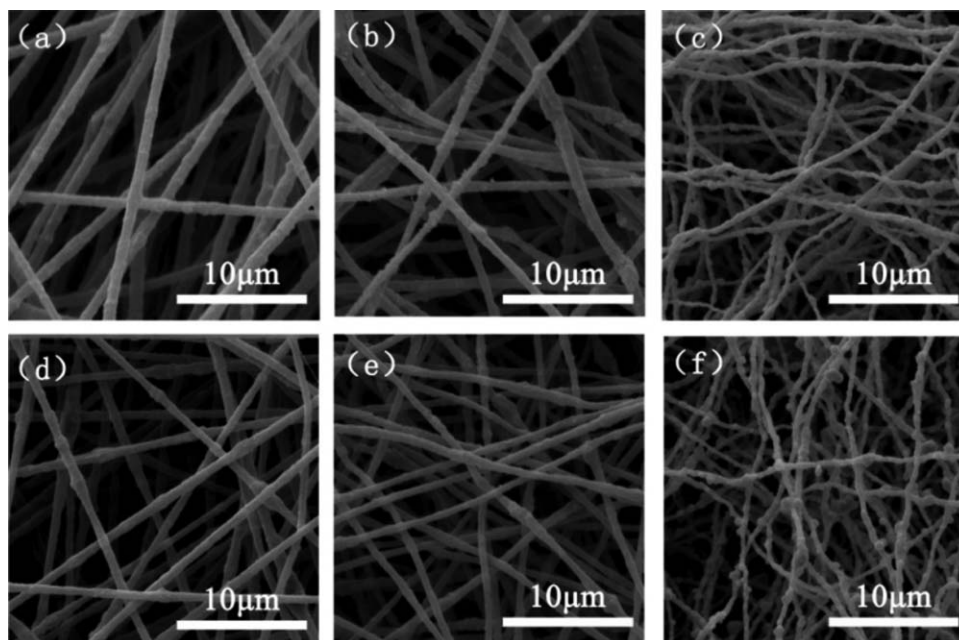
Table III. Main Thermal Decomposition Temperatures in the Thermal Curves of the Electrospun LiFePO$_4$ Precursor–PAN and LiFePO$_4$ Precursor–PAN–MWCNT3 Composites after Stabilization in N$_2$

Sample	TGA	DTA
Stabilized LiFePO$_4$ precursor–PAN (°C)	350–800 and 800–900	446, 575, and 825
Stabilized LiFePO$_4$ precursor–PAN–MWCNT3 (°C)	350–800 and 800–900	446 and 825

Figure 4. Scanning electron microscopy images of the (a) electrospun LiFePO$_4$ precursor–PAN, (b) electrospun LiFePO$_4$ precursor–PAN after stabilization, (c) LiFePO$_4$–CNF, (d) electrospun LiFePO$_4$ precursor–PAN–MWCNT3, (e) electrospun LiFePO$_4$ precursor–PAN–MWCNT3 after stabilization, and (f) LiFePO$_4$–CNF–MWCNT3 composites.

were observed. However, after thermal treatment, the fiber diameters decreased; this led to the exposure of the aggregated LiFePO$_4$ clusters and MWCNTs. In addition, during the thermal treatment process, the LiFePO$_4$ precursors went through complex reactions; these may have generated larger LiFePO$_4$ particles and resulted in some LiFePO$_4$ particles attaching to the fibers and others embedding in the fibers. The particle size and

size distribution should have somehow affected the electrochemical properties.

Structural Characterization

The carbon contents of the LiFePO$_4$–CNF and LiFePO$_4$–CNF–MWCNT composites were determined. They were found to be 17.10, 17.46, 17.72, 18.02, 18.46, 19.27, and 20.45 wt %,
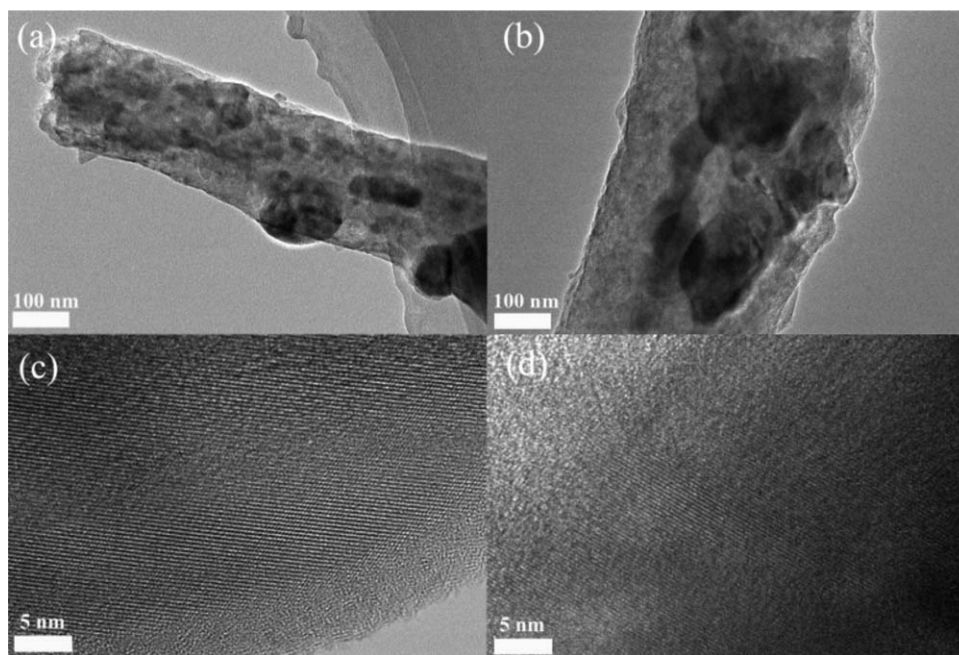

Figure 5. TEM images of the (a) LiFePO$_4$–CNF and (b) LiFePO$_4$–CNF–MWCNT3 composites. HRTEM images of the (c) LiFePO$_4$–CNF and (d) LiFePO$_4$–CNF–MWCNT3 composites.
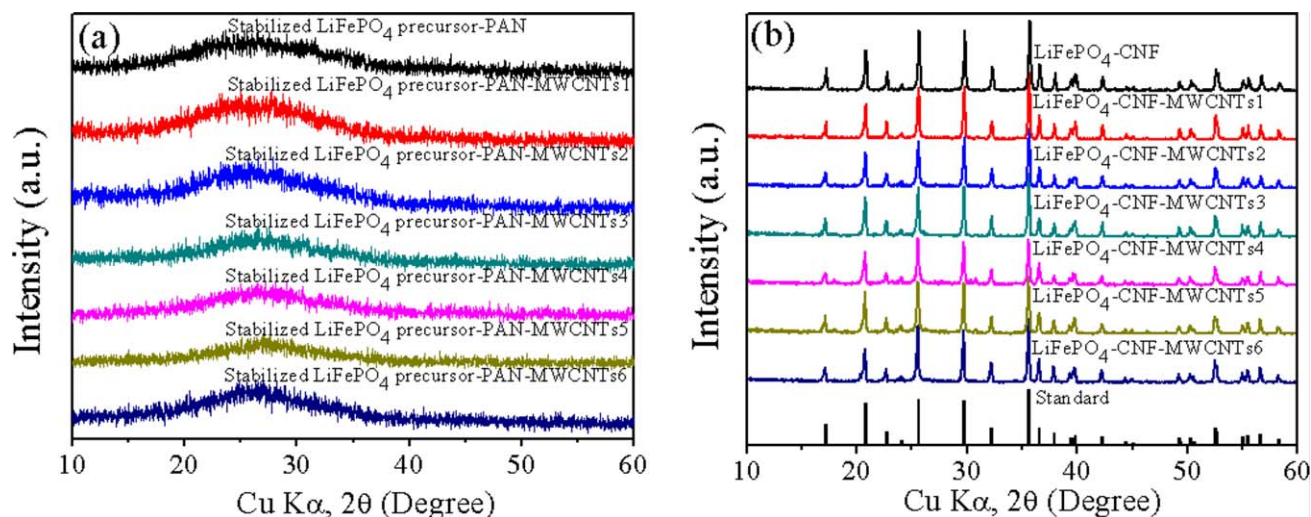
Figure 6. XRD patterns of the (a) electrospun LiFePO$_4$ precursor–PAN and LiFePO$_4$ precursor–PAN–MWCNT composites after stabilization and (b) LiFePO$_4$–CNF and LiFePO$_4$–CNF–MWCNT composites. The reflections of LiFePO$_4$ (card number 81-1173) are shown in panel b for comparison. [Color figure can be viewed in the online issue, which is available at wileyonlinelibrary.com.]

respectively, for the LiFePO$_4$–CNF, LiFePO$_4$–CNF–MWCNT1, LiFePO$_4$–CNF–MWCNT2, LiFePO$_4$–CNF–MWCNT3, LiFePO$_4$–CNF–MWCNT4, LiFePO$_4$–CNF–MWCNT5, and LiFePO$_4$–CNF–MWCNT6 composites.

Figure 5 shows the transmission electron microscopy (TEM) and HRTEM microphotographs of the LiFePO$_4$–CNF and LiFePO$_4$–CNF–MWCNT3 composites. TEM [Figure 5(a,b)] showed that the sample was made up of the active materials and carbon mixed relatively uniformly in the nanofibers. HRTEM [Figure 5(c,d)] was performed to observe the carbon layer and structural information of the LiFePO$_4$ active materials. Figure 5(c,d) presents a uniform carbon layer on the surfaces of the sample. The carbon in the materials not only prevented the active materials from aggregating but also improved the electrical conductivity of the composites. Additionally, the HRTEM photographs exhibited reasonable lattice fringes.

The XRD curves of the electrospun composites after stabilization and carbonation are shown in Figure 6. We observed that for all of the composites after stabilization [Figure 5(a)], there was one broad and small diffraction peak; this indicated that the amorphous phase was present after stabilization. Figure 5(b) shows the XRD patterns of all of the composites after carbonization. The standard card data of LiFePO$_4$ is also shown in

Figure 5(b). We observed that all of the XRD patterns of composites were identified as an olivine LiFePO$_4$ with an orthorhombic crystal structure in the Pnma space group (card number 81-1173, $a = 10.332$ Å, $b = 6.010$ Å, $c = 4.692$ Å, $V = 291.35$ Å^3; where a, b and c are lattice parameters of cell, V is the lattice volume of cell), and there was no impurity phase. The profiles of the main reflection peak were sharp; this indicated that the crystallite LiFePO$_4$ developed very well. No peaks corresponding to carbon were observed in the XRD pattern, possibly because of its low content. The lattice parameters and unit cell volumes of the LiFePO$_4$–CNF and LiFePO$_4$–CNF–MWCNT composites are given in Table IV. All of the values were in good agreement with the standard card data. In comparison with those of the LiFePO$_4$–CNF composites, the XRD patterns and unit cell volumes of the LiFePO$_4$–CNF–MWCNT composites were almost unchanged. This indicated that addition of MWCNTs into the precursor did not change the olivine structure of LiFePO$_4$.

Raman Spectra

Raman spectroscopy is an important assistant for investigating the properties of the carbon phase, which are not detected by XRD. The obtained Raman spectra of the electrospun LiFePO$_4$ precursor–PAN, electrospun LiFePO$_4$ precursor–PAN–

Table IV. Lattice Parameters and Unit Cell Volumes of the LiFePO$_4$–CNF and LiFePO$_4$–CNF–MWCNT Composites

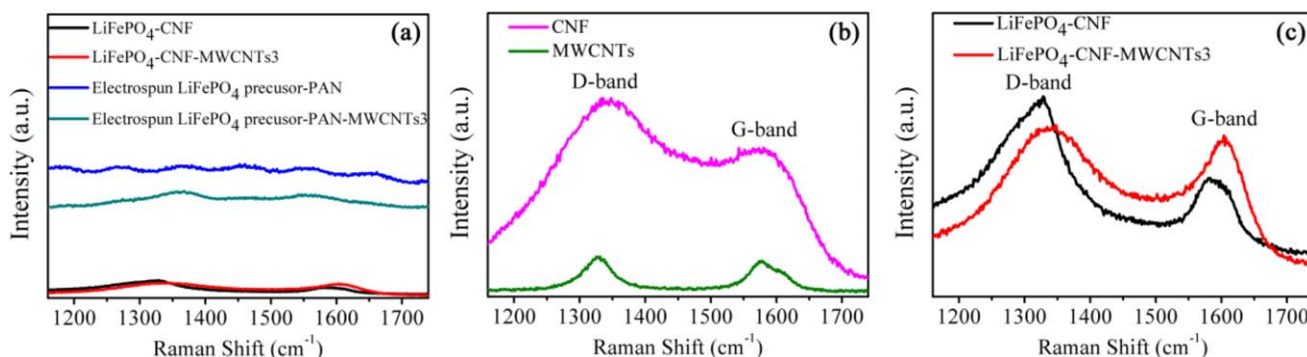| Sample	a (Å)	b (Å)	c (Å)	V (Å^3)
LiFePO$_4$–CNF	10.313	5.994	4.685	289.65
LiFePO$_4$–CNF–MWCNT1	10.322	6.001	4.688	290.40
LiFePO$_4$–CNF–MWCNT2	10.317	6.003	4.687	290.30
LiFePO$_4$–CNF–MWCNT3	10.332	6.010	4.692	291.35
LiFePO$_4$–CNF–MWCNT4	10.332	6.010	4.692	291.35
LiFePO$_4$–CNF–MWCNT5	10.332	6.010	4.692	291.35
LiFePO$_4$–CNF–MWCNT6	10.332	6.010	4.692	291.35

Figure 7. Raman spectra of the electrospun LiFePO$_4$ precursor–PAN, electrospun LiFePO$_4$ precursor–PAN–MWCNT3, CNFs, MWCNTs, LiFePO$_4$–CNF, and LiFePO$_4$–CNF–MWCNT3. [Color figure can be viewed in the online issue, which is available at wileyonlinelibrary.com.]

MWCNT3, CNFs, MWCNTs, LiFePO$_4$–CNF, and LiFePO$_4$–CNF–MWCNT3 composites are shown in Figure 7. The characteristic Raman bands of these sample are shown in Table V. The D band (disorder-induced mode, 1250–1450 cm^{-1}) was induced by defects and disordered portions in the graphitic lattice, and its origin was explained by double-resonant Raman scattering. The G band [ordered-induced mode (E$_{2g2}$)] graphitic mode, 1550–1600 cm^{-1}) was attributed to the ideal ordered graphitic lattice vibration mode.[46,47] The exact positions of the bands depended on the laser frequency and the details of the electronic and phonon energy dispersion. The relative peak intensity ratio of the D band and G band (I_D/I_G) were used to analyze the number of carbon defects in the composites. This was in inverse proportion to the graphitization degree of carbon. Therefore, a smaller I_D/I_G ratio indicated the presence of a larger amount of graphitic crystallites of carbon as compared to the disordered portions of carbon.[48–51]

The Raman spectra of the electrospun webs before and after the thermal treatments are shown in Figure 7(a). We observed that the Raman spectrum of the electrospun LiFePO$_4$ precursor–PAN fluctuated most because of the existence of the PAN, LiCOOCH$_3$, Fe(COOCH$_3$)$_2$, and H$_3$PO$_4$ components. When the MWCNTs were added, the Raman spectrum of the LiFePO$_4$ precursor–PAN–MWCNT3 showed the D band and G band. After thermal treatment, the LiFePO$_4$ precursor–PAN changed to LiFePO$_4$–CNF, and the spectrum showed obvious D and G bands because of the presence of CNFs. When the LiFePO$_4$ precursor–PAN–MWCNT3 was converted into LiFePO$_4$–CNF–MWCNT3, the spectrum exhibited the D and G bands as well.

As shown in Figure 7(b) and Table V, the obtained CNFs showed two broad bands around 1334 and 1573 cm^{-1}; these

were ascribed to the D and G bands. For the MWCNTs, two broad bands were detected at 1331 and 1578 cm^{-1}, respectively. The position for the peaks of the D and G peaks showed a difference for the CNFs and MWCNTs; this was due to the differences between the MWCNT and CNF microstructures, such as the quantum-size effect of the MWCNTs with hollow centers. In addition, the I_D/I_G ratio of the obtained CNFs was calculated to be 1.201 and that of the MWCNTs was calculated to be 1.116. This indicated that the MWCNTs had higher degrees of order and graphitization than the CNFs.

As shown in Figure 7(c) and Table V, the obtained LiFePO$_4$–CNF composites showed two broad bands around 1328 and 1581 cm^{-1}. For the LiFePO$_4$–CNF–MWCNT3 composites, two broad bands were detected at 1348 and 1603 cm^{-1}. A closer look at the spectrum indicated that the bands were shifted to lower frequencies in the LiFePO$_4$–CNF–MWCNT composites compared to the LiFePO$_4$–CNF composite. Different positions for the sample peaks of the D and G bands usually indicate different carbon structures in the samples. There was a difference for the CNFs and MWCNTs [Figure 7(b)]; therefore, there was no doubt that the shift was related to surface effects involving the bonding of the LiFePO$_4$ particle surface with MWCNTs. As shown in Table V, the I_D/I_G ratio of the obtained LiFePO$_4$–CNF composites was calculated to be 1.688, and the I_D/I_G ratio of the obtained LiFePO$_4$–CNF–MWCNT3 composites was calculated to be 1.065. The I_D/I_G ratio decreased from 1.688 to 1.065 with the addition of MWCNTs into the precursor. This indicated that the composite materials with the presence of MWCNTs contained more ordered carbon structures. The results correlated well with the CNFs and MWCNTs, as shown in Figure 7(b). The higher degree of graphitization indicated the higher electronic conductivity of the residual carbon.

Initial Charge–Discharge Profiles and Cycle Performance
Typical galvanostatic initial charge–discharge curves and the cycle performance of LiFePO$_4$–CNF and LiFePO$_4$–CNF–MWCNT composites are shown in Figure 8(a,b), respectively. The composites exhibited good reversibility during the lithium intercalation–deintercalation process.

As shown in Figure 8(a), during the first cycle, the composites with and without MWCNTs showed similar flat voltage plateaus around 3.5 and 3.4 V, respectively, for charging and discharging;
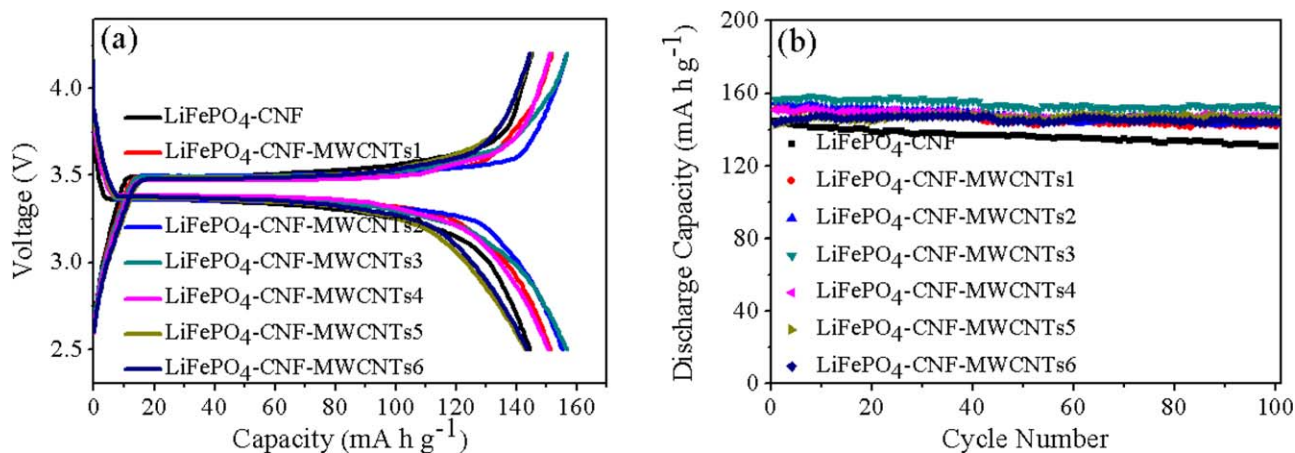
Table V. Characteristic Raman Bands of the CNFs, MWCNTs, LiFePO$_4$–CNF, and LiFePO$_4$–CNF–MWCNT3 Composites

Sample	D peak (cm^{-1})	G peak (cm^{-1})	I_D/I_G
CNFs	1334	1573	1.201
MWCNTs	1331	1578	1.116
LiFePO$_4$–CNF	1328	1581	1.688
LiFePO$_4$–CNF–MWCNT3	1348	1603	1.065

Figure 8. (a) Initial charge–discharge curves and (b) cycle performances of LiFePO4–CNF and LiFePO4–CNF–MWCNT composites at a charge–discharge rate of 0.5 C. [Color figure can be viewed in the online issue, which is available at wileyonlinelibrary.com.]

this was characteristic behavior of the two-phase reaction of LiFePO4. There was a slight difference in the charge–discharge plateau voltage, which was attributed to the polarization of the cathode. Also, the initial discharge-specific capacities were 144.4, 151.2, 155.2, 156.7, 150.5, 142.8, and 143.5 mA h g^{-1} for the LiFePO4–CNF, LiFePO4–CNF–MWCNT1, LiFePO4–CNF–MWCNT2, LiFePO4–CNF–MWCNT3, LiFePO4–CNF–MWCNT4, LiFePO4–CNF–MWCNT5, and LiFePO4–CNF–MWCNT6 composites, respectively. This may not have been so statistically significant.

The cycling performances of the composites with and without MWCNTs are shown in Figure 8(b). The discharge capacities remained relatively sustainable for the LiFePO4–CNF–MWCNT composites during 100 cycles at a charge–discharge rate of 0.5 C, and that for the LiFePO4–CNF composites faded slightly. This may have been due to the fact that the intertwined MWCNTs could protect the electrode from failure and alleviate electrolyte decomposition. The incorporation of the MWCNTs provided additional highly conductive bridges between particles, and this led to the availability of a conduction path. These resulted in a greater electrochemical efficiency. Among all of the

loaded MWCNT composites, LiFePO4–CNF–MWCNT3 showed the best performance.

Rate Performance

Figure 9 gives information on the rate performance of the composites with and without MWCNTs. The LiFePO4–CNF–MWCNT composites exhibited a satisfactory rate capability compared with the LiFePO4–CNF composites, when the rate increased from 0.05 to 2 C. This provided further evidence for the importance of MWCNTs existing in the samples. This excellent rate performance was partially attributed to the higher electronic conductivity and lithium-ion diffusion of the composites. The CNFs had small fiber diameters; this shortened the lithium-ion diffusion pathway, enhanced the electrode reaction kinetics, and reduced the polarization. The porous microstructure and large surface area of the MWCNTs provided many transport passages for the lithium ions and electrons, formed conducting bridges between the particles, and increased the electrical conductivity of the system. These synergic effects of the CNFs and MWCNTs provided satisfactory rate capabilities when the LiFePO4–CNF–MWCNT composites were used as cathodes in LIBs. Among all of the composites, the composites containing

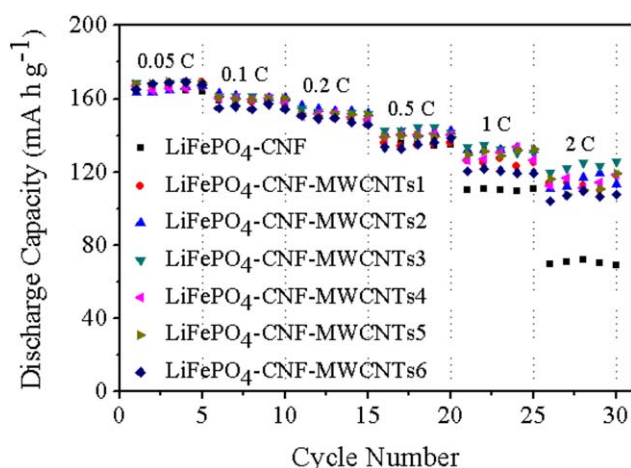**Figure 9.** Rate capabilities of the LiFePO4–CNF and LiFePO4–CNF–MWCNT composites at a charge rate of 0.05 C. [Color figure can be viewed in the online issue, which is available at wileyonlinelibrary.com.]

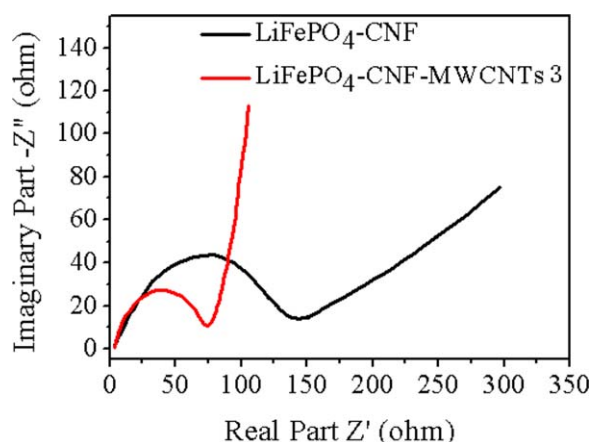**Figure 10.** EIS spectra of the LiFePO4–CNF and LiFePO4–CNF–MWCNT3 composites. [Color figure can be viewed in the online issue, which is available at wileyonlinelibrary.com.]

0.15 wt % MWCNTs exhibited the best performance. The average reversible capacities obtained were as follows: 168.2, 160.7, 152.6, 143.1, 132.4, and 123.2 mA h g^{-1}, for discharge rates of 0.05, 0.1, 0.2, 0.5, 1, and 2C, respectively. This showed good correlation with the cycling performance, as shown in Figure 8. This may have been due to the fact that the greater number of MWCNTs prevented the electrolyte from entering the inside of the active materials. There needs to be a balance between the properties and the loaded amount of MWCNTs.

EIS Analysis

EIS measurement was carried out to further understand the effect of the MWCNTs on the kinetic process of the composites. The EIS profiles of the LiFePO$_4$–CNF and LiFePO$_4$–CNF–MWCNT3 composites are shown in Figure 10. The spectra were composed of a depressed semicircle in the high-frequency region; this was related to the charge-transfer resistance for the lithiation reaction at the interface of the electrolyte and cathode, and the sloping straight line in the low-frequency region corresponded to the Warburg impedance, which was related to the lithium-ion diffusion process within the cathode.[52] In the high-frequency region, a smaller diameter semicircle reflected a lower charge-transfer impendence at the interface of the electrolyte and cathode. According to the results, the MWCNT-loaded composites exhibited almost half of the charge-transfer resistance for the LiFePO$_4$–CNF composites. This indicated that charge transfer at the interface of the electrolyte and cathode materials was obviously accelerated by the addition of the MWCNTs. In the low-frequency region, the slope of the straight line for the MWCNT-loaded composites was larger than that for LiFePO$_4$–CNF; this indicated that the composites with MWCNTs were more favorable for the transport of lithium ions. This was also in agreement with the results of the cycling performance and rate capability.

CONCLUSIONS

LiFePO$_4$–CNF–MWCNT composites were prepared as binder-free cathode materials for LIBs by electrospinning and thermal treatment. Nanosized LiFePO$_4$ materials were synthesized *in situ* with the encapsulation of the conductive CNF matrix; simultaneously, the MWCNTs were embedded in the LiFePO$_4$–CNF matrix. This formed a freestanding conductive web that could be used directly as a battery cathode without the addition of a conductive material and polymer binder. All of the electrospun composites maintained their networklike structures after the thermal treatment. The XRD, TEM, and HRTEM results show that the materials had an olivine structure. MWCNT-loaded LiFePO$_4$–CNF composites are very promising for next-generation LIBs in terms of a more stable cycling performance, better rate capabilities, and lower charge-transfer resistance. The composites containing 0.15 wt % MWCNTs were shown to have the best electrochemical performance among all of the composites.

ACKNOWLEDGMENTS

REFERENCES

1. Liu, J.; Liu, X.-W. *Adv. Mater.* **2012**, *24*, 4097.
2. Armand, M.; Tarascon, J. M. *Nature* **2008**, *451*, 652.
3. Fergus, J. W. *J. Power Sources* **2010**, *195*, 939.
4. Gibot, P.; Casas-Cabanas, M.; Laffont, L.; Levasseur, S.; Carlach, P.; Hamelet, S.; Tarascon, J.-M.; Masquelier, C. *Nat. Mater.* **2008**, *7*, 741.
5. Yoo, H.; Jo, M.; Jin, B.-S.; Kim, H.-S.; Cho, J. *Adv. Energy Mater.* **2011**, *1*, 347.
6. Kim, H.; Park, I.; Seo, D.-H.; Lee, S.; Kim, S.-W.; Kwon, W. J.; Park, Y.-U.; Kim, C. S.; Jeon, S.; Kang, K. *J. Am. Chem. Soc.* **2012**, *134*, 10369.
7. Padhi, A. K.; Nanjundaswamy, K. S.; Goodenough, J. B. *J. Electrochem. Soc.* **1997**, *144*, 1188.
8. Yang, S. F.; Zavalij, P. Y.; Whittingham, M. S. *Electrochem. Commun.* **2001**, *3*, 505.
9. Zhao, Y.; Peng, L.; Liu, B.; Yu, G. *Nano Lett.* **2014**, *14*, 2849.
10. Zhong, K.; Cui, Y.; Xia, X.; Xue, J.; Liu, P.; Tong, Y. *J. Power Sources* **2014**, *250*, 296.
11. Mei, R.; Song, X.; Yang, Y.; An, Z.; Zhang, J. *RSC Adv.* **2014**, *4*, 5746.
12. Wang, F.; Chen, J.; Tan, Z.; Wu, M.; Yi, B.; Su, W.; Wei, Z.; Liu, S. *J. Taiwan Inst. Chem. Eng.* **2014**, *45*, 1321.
13. Konarova, M.; Taniguchi, I. *J. Power Sources* **2010**, *195*, 3661.
14. Hsu, K. F.; Tsay, S. Y.; Hwang, B. J. *J. Mater. Chem.* **2004**, *14*, 2690.
15. Gao, M.; Liu, N.; Li, Z.; Wang, W.; Li, C.; Zhang, H.; Chen, Y.; Yu, Z.; Huang, Y. *Solid State Ionics* **2014**, *258*, 8.
16. Yu, S.; Kim, S.; Kim, T. Y.; Nam, J. H.; Cho, W. I. *J. Appl. Electrochem.* **2013**, *43*, 253.
17. Zhou, Y.; Wang, J.; Hu, Y.; O'Hayre, R.; Shao, Z. *Chem. Commun.* **2010**, *46*, 7151.
18. Liu, J.; Conry, T. E.; Song, X.; Doeff, M. M.; Richardson, T. J. *Energy Environ. Sci.* **2011**, *4*, 885.
19. Cheng, F.; Wang, S.; Wang, C.-Y.; Li, W.-C. *Micropor. Mesopor. Mater.* **2015**, *204*, 190.
20. Meethong, N.; Kao, Y.-H.; Speakman, S. A.; Chiang, Y.-M. *Adv. Funct. Mater.* **2009**, *19*, 1060.
21. Omenya, F.; Chernova, N. A.; Wang, Q.; Zhang, R.; Whittingham, M. S. *Chem. Mater.* **2013**, *25*, 2691.
22. Subramanya Herle, P.; Ellis, B.; Coombs, N.; Nazar, L. F. *Nat. Mater.* **2004**, *3*, 147.
23. Talebi-Esfandarani, M.; Savadogo, O. *J. Appl. Electrochem.* **2014**, *44*, 555.

24. Zhang, C.; Liang, Y.; Yao, L.; Qiu, Y. *Solid State Ionics* **2014**, *267*, 74.

25. Yang, X.; Mou, F.; Zhang, L.; Peng, G.; Dai, Z.; Wen, Z. *J. Power Sources* **2012**, *204*, 182.

26. Liu, Y.; Xu, Y.; Han, X.; Pellegrinelli, C.; Zhu, Y.; Zhu, H.; Wan, J.; Chung, A. C.; Vaaland, O.; Wang, C.; Hu, L. *Nano Lett.* **2012**, *12*, 5664.

27. Fan, Q.; Lei, L.; Xu, X.; Yin, G.; Sun, Y. *J. Power Sources* **2014**, *257*, 65.

28. Van Hiep, N.; Gu, H.-B. *J. Appl. Electrochem.* **2014**, *44*, 1153.

29. Lei, X.; Zhang, H.; Chen, Y.; Wang, W.; Ye, Y.; Zheng, C.; Deng, P.; Shi, Z. *J. Alloy. Compd.* **2015**, *626*, 280.

30. Mei, R.; Yang, Y.; Song, X.; An, Z.; Zhang, J. *Electrochim. Acta* **2015**, *153*, 523.

31. Hsieh, C.-T.; Pai, C.-T.; Chen, Y.-F.; Chen, I. L.; Chen, W.-Y. J. *Taiwan Inst. Chem. Eng.* **2014**, *45*, 1501.

32. Qiu, L.; Shao, Z.; Wang, W.; Wang, F.; Wang, J.; Wang, D.; Wang, Y. *Electrochim. Acta* **2014**, *145*, 11.

33. Jiang, C.; Saha, A.; Young, C. C.; Hashim, D. P.; Ramirez, C. E.; Ajayan, P. M.; Pasquali, M.; Marti, A. A. *ACS Nano* **2014**, *8*, 9107.

34. Qiu, L.; Shao, Z.; Yang, M.; Wang, W.; Wang, F.; Wan, J.; Wang, J.; Bi, Y.; Duan, H. *Cellulose* **2014**, *21*, 615.

35. Chen, J. J.; Whittingham, M. S. *Electrochem. Commun.* **2006**, *8*, 855.

36. Chen, M.; Du, C.; Song, B.; Xiong, K.; Yin, G.; Zuo, P.; Cheng, X. *J. Power Sources* **2013**, *223*, 100.

37. Jin, B.; Jin, E. M.; Park, K.-H.; Gu, H.-B. *Electrochem. Commun.* **2008**, *10*, 1537.

38. Gnanavel, M.; Patel, M. U. M.; Sood, A. K.; Bhattacharyya, A. J. *J. Electrochem. Soc. A* **2012**, *159*, 336.

39. Qin, G.; Ma, Q.; Wang, C. *Solid State Ionics* **2014**, *257*, 60.

40. Toprakci, O.; Toprakci, H. A. K.; Ji, L.; Xu, G.; Lin, Z.; Zhang, X. *ACS Appl. Mater. Interfaces* **2012**, *4*, 1273.

41. Wang, D. Y.; Hong, L.; Wang, Z. X.; Wu, X. D.; Sun, Y. C.; Huang, X. J.; Chen, L. Q. J. *Solid State Chem.* **2004**, *177*, 4582.

42. Yu, F.; Zhang, J.; Yang, Y.; Song, G. *Electrochim. Acta* **2009**, *54*, 7389.

43. Rahaman, M. S. A.; Ismail, A. F.; Mustafa, A. *Polym. Degrad. Stab.* **2007**, *92*, 1421.

44. Fitzer, E. *Carbon* **1989**, *27*, 621.

45. Liu, J.; Tang, K.; Song, K.; van Aken, P. A.; Yu, Y.; Maier, J. *Phys. Chem. Chem. Phys.* **2013**, *15*, 20813.

46. Graupner, R. *J. Raman Spectrosc.* **2007**, *38*, 673.

47. Reich, S.; Thomsen, C. *Philos. Trans. R. Soc. London Ser. A* **2004**, *362*, 2271.

48. Ji, L.; Yao, Y.; Toprakci, O.; Lin, Z.; Liang, Y.; Shi, Q.; Medford, A. J.; Millns, C. R.; Zhang, X. *J. Power Sources* **2010**, *195*, 2050.

49. Kim, C.; Jeong, Y. I.; Ngoc, B. T. N.; Yang, K. S.; Kojima, M.; Kim, Y. A.; Endo, M.; Lee, J.-W. *Small* **2007**, *3*, 91.

50. Kim, C.; Yang, K. S.; Kojima, M.; Yoshida, K.; Kim, Y. J.; Kim, Y. A.; Endo, M. *Adv. Funct. Mater.* **2006**, *16*, 2393.

51. Morales-Teyssier, O.; Sanchez-Valdes, S.; Ramos-de Valle, L. F. *Macromol. Mater. Eng.* **2006**, *291*, 1547.

52. Lin, Y.; Pan, H.; Gao, M.; Liu, Y. J. *Electrochem. Soc. A* **2007**, *154*, 1124.